The Effect of Grid Topology on Transient Fault Currents in Multi-Terminal VSC-HVDC Offshore Networks

M. D. Pfeiffer, M. K. Bucher, C. M. Franck

***Abstract*– This paper investigates different network topologies of potential future DC offshore grids with respect to their impact on transient fault currents for permanent single pole-to-ground faults. Investigations are carried out on a twelve-terminal $\pm 320\,$kV VSC-HVDC network modeled around the physical topology of the North Sea. Results are obtained through EMTP simulations in PSCAD using a detailed, frequency-dependent model of an XLPE-insulated HVDC submarine cable. Four distinct grid topologies are considered. The obtained results suggest that topologies that are advantageous for system redundancy and flexible trading, i.e. meshed networks, may be disadvantageous from a maximum fault current point of view. Densely meshed grids do not only lead to higher fault currents, but also pose a serious challenge in the first few ms due to high discharge currents of cable capacitances. Results are discussed in relation to the performance of modern HVDC steady-state hybrid circuit breakers and mechanical passive resonance breakers. They suggest that the faster interruption speed of the former might lead to lower breaking current requirements.**

***Keywords*: multiterminal VSC HVDC, offshore wind power, offshore grids, fault transients.**

I. Introduction

Voltage Source Converter (VSC) based High Voltage Direct Current (HVDC) power transmission has been successfully implemented in a number of offshore power transmission projects [1], [2]. Under certain conditions, VSC-HVDC is the only viable offshore transmission option, i.e. if long transmission distances exist in combination with environmental concerns about oil filled cables (as used in traditional HVDC), space requirements, or weak AC connection points.

In the future, VSC technology may also play a key role in enabling multi-terminal HVDC (MTDC) grids, the implementation of which is facilitated by VSC's ability to reverse the power flow direction without reversing the polarity [3]. A major unresolved issue with regard to MTDC grids remains their protection against DC side faults [4]–[7]. Passive discharges from DC-side filter and cable capacitances, combined with fault current contributions from connected AC nodes, can lead to very severe fault transients, which pose significant demands on future HVDC protection systems. Factors that determine the nature of these transients include the characteristics of the VSC converter, the DC grid's grounding scheme and the characteristics of connected AC grid points.

Another key factor is the DC grid topology. This aspect has not received much attention in the literature yet and is the focus of this paper. Using the example of a twelve-terminal North Sea grid connecting six northern European countries and three offshore clusters, this paper investigates key dependencies between the DC grid topology and transient fault currents through DC circuit breakers (DC CBs) for different fault locations and grid structures.

Results are obtained through EMTP simulations in PSCAD based on equivalent models of onshore and offshore coupling points, converter stations, and frequency-dependent distributed-parameter cable representations.

The paper is structured as follows: Section II outlines the main characteristics of the system model. Section III describes the different grid and fault scenarios. Section IV presents and discusses simulation results. Finally, Section V concludes with a discussion of the obtained results and their implications for the design of future offshore networks.

II. Grid Component Modeling

A. Converter Stations and Coupling Points

Each VSC-HVDC converter station in the DC grid is assumed to be a bipole two-level converter with a nominal rating of 900 MW operating at $\pm 320\,$kV. In order to reduce the computation time, however, only the positive pole is considered and the converter stations are thus modeled as asymmetrical monopoles as shown in Fig. 1. The connected AC network is modeled as a constant voltage source behind a grid impedance.

The converters are modeled under the assumption that in the case of a fault, the IGBTs switch off instantaneously for self-protection (the same assumption as in [8]). This means that the model in Fig. 1 can be implemented as a simple uncontrolled diode rectifier, i.e. without modeling the IGBTs. Small concentrated filter capacitances, C_f, of $1\,\mu F$ are assumed.

B. Cables

A distributed-parameter cable representation based on the frequency-dependent phase model in PSCAD was implemented. The general design of the cable is based on information in [1], [9], [10] about the $\pm 150\,$kV XLPE insulated submarine cable installed in the Estlink HVDC connection

The project is financially supported by ABB Switzerland Ltd, Siemens AG, Alstom Grid, and the Swiss Federal Office of Energy (BfE).

M. D. Pfeiffer, M. K. Bucher and C. M. Franck are with the Power Systems and High Voltage Laboratories, ETH Zurich, 8092 Zurich, Switzerland (e-mail: pfeiffer, bucher, franck@eeh.ee.ethz.ch).

Paper submitted to the International Conference on Power Systems Transients (IPST2013) in Vancouver, Canada, July 18-20, 2013.

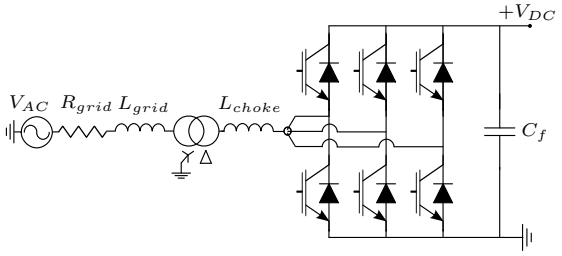

Fig. 1. Model of AC coupling point and asymmetrical monopole converter.

between Estonia and Finland. The cable parameters were scaled up to 320 kV based on data in [11]. The resulting dimensions and material properties (based on values in [12]) are given in Table I. A scaled drawing of the cross-section is shown in Fig. 2.

TABLE I
PROPERTIES OF ASSUMED 320 KV XLPE INSULATED HVDC SUBMARINE CABLE

Layer	Material	Outer radius (mm)	Resistivity (Ωm)	Rel. permittivity	Rel. permeability
(1) Core	Copper	21.4	1.72×10^{-8}	1	1
(2) Insulation	XLPE	45.9	-	2.3	1
(3) Sheath	Lead	49.4	2.2×10^{-7}	1	1
(4) Insulation	XLPE	52.4	-	2.3	1
(5) Armor	Steel	57.9	1.8×10^{-7}	1	10
(6) Insulation	PP	61.0	-	2.1	1

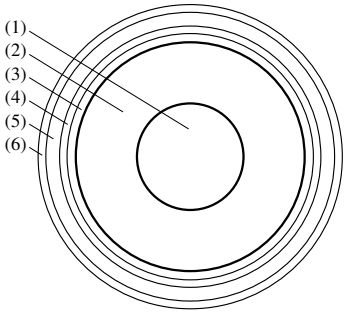

Fig. 2. Cross-section of assumed 320 kV XLPE insulated HVDC submarine cable.

C. Offshore Coupling Points

Because most offshore wind farms will be based on variable speed turbines that are connected to the grid through full-power frequency converters [13], a distinct representation of offshore coupling points is employed. There is a relatively broad consensus in the scientific literature regarding the nature and magnitude of the short circuit current contribution from full converter wind turbines. In [14]–[19], it is stated that their fault current contribution is limited to the turbine's nominal current or a value slightly above it. It is also generally agreed that the short circuit current contribution depends primarily on the characteristics of the converter rather than the physical properties of the generator.

The offshore nodes were thus modeled in a slightly different manner than the regular onshore AC nodes. The implementation leans on the approach in [20], in which the initial symmetrical short circuit current contribution of full converter wind turbines is modeled as:

$$I_{\mathrm{SC}} = kI_{\mathrm{rG}} \quad , \tag{1}$$

where k is the factor by which the short circuit current exceeds the nominal current of the wind turbine. This approach was modified to account for initial transients reported in [18] and [19]. The resulting model is implemented in the form of a voltage source with a variable short circuit power. Based on the information provided in [18], k is chosen to decrease from 3 to 1.5 over the duration of two cycles (i.e. 40 ms) after the fault initiation and subsequently remains constant. For lack of more detailed information, a linear transition between the two values was chosen [13].

III. Grid Parameters and Scenarios

A. Coupling Point Characteristics

A detailed twelve-terminal VSC HVDC grid model, consisting of 9 onshore and 3 offshore nodes, was built around the geography of the North Sea (Fig. 3). The location of onshore coupling points was derived from existing plans for offshore grids in the North Sea [21], [22], while also considering the location of existing high voltage substations as given on the ENTSO-E Grid Map [23]. The locations of the three offshore nodes are roughly based on the location of approved zones in which licenses for large scale offshore wind farms have been granted. Tables II and III summarize key parameters of the nodes. The point of common coupling (PCC) voltage values correspond to the highest AC voltage level in each of the connected countries. The short circuit values, S_{SC}, lean on assumptions made in [24] regarding the maximum short circuit current in the Spanish high voltage grid. The assumptions of the reactance to resistance ratio, X/R, lean on values given for high voltage networks in [25].

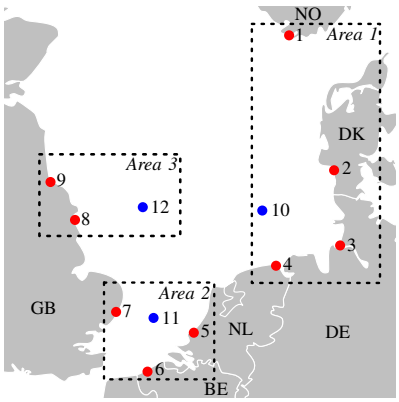

Fig. 3. Offshore grid node locations and numbering.

B. Grid Topologies

The four grid topologies under investigation are shown in Fig. 4. Connection distances are given in Table IV. The rationale behind each topology is briefly described in the following paragraphs:

TABLE II
PARAMETERS OF ONSHORE NODES

Node #	Country	PCC Voltage (kV)	S_{SC} (MVA)	X/R
1	NO	300	23400	8.5
2	DK	380	26300	10
3	DE	380	26300	10
4	NL	380	26300	10
5	NL	380	26300	10
6	BE	380	26300	10
7	UK	400	27700	10
8	UK	400	27700	10
9	UK	400	27700	10

TABLE III
PARAMETERS OF OFFSHORE NODES

Node #	Concession Area	Nameplate Capacity (MW)
10	BARD Area	4000
11	Norfolk Bank	3600
12	Dogger Bank	4500

a) Radial Grid: This topology consists of a series connection of all three offshore nodes and radial connections from the offshore nodes to the onshore nodes in their zone. In principal, all individual countries can trade with each other.

b) Lightly Meshed Grid: This topology extends the linear connection between the three offshore nodes with another offshore connection between nodes 10 and 11. This creates an N-1 level of redundancy in terms of power transfer between the three zones. Furthermore, the flexibility with regard to power trading is enhanced. For example, Norway could export power to Belgium, while at the same time Denmark imports power from the UK (this is not feasible in grid (a)).

c) Ring Shaped Grid: In this topology, the three areas are connected with each other at their periphery. The full capacity of each inter-area connection can be scheduled independently of wind power evacuation requirements.

d) Densely Meshed Grid: This topology consists of the largest number of connections and represents the highest level of redundancy and flexibility among the four topologies. Furthermore, because the average transmission distance between any two given points in this system is shortest, this scenario would also be expected to lead to the lowest system losses [26]. It is of course also associated with the highest investment costs.

TABLE IV
CONNECTION DISTANCES IN TWELVE TERMINAL OFFSHORE GRID TOPOLOGIES

From	To	Distance (km)	From	To	Distance (km)
1	9	595	6	7	145
1	10	405	6	11	145
1	12	465	7	8	240
2	4	240	7	11	100
2	9	610	8	12	180
2	10	155	9	12	210
3	10	185	10	11	320
4	10	135	10	12	290
4	5	280	11	12	295
5	11	95			

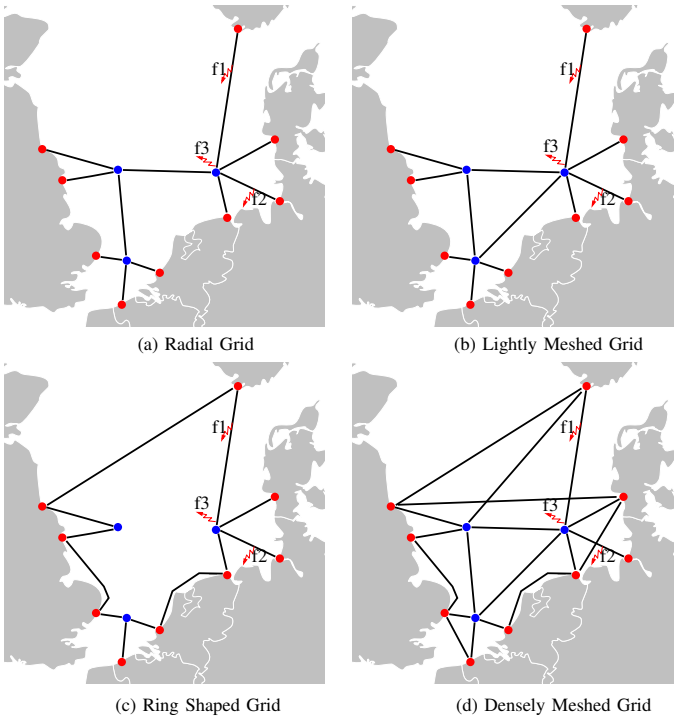

(a) Radial Grid (b) Lightly Meshed Grid

(c) Ring Shaped Grid (d) Densely Meshed Grid

Fig. 4. Four different considered grid topologies.

C. Fault Scenarios

Faults f1 and f2 (c.f. Fig. 4) are applied to connections between offshore node 10 and onshore nodes 1 and 3, respectively. Fault f1 is 100 km away from node 1 and f2 is 85 km away from node 3. The primary difference between the two fault locations is that f2 is directly next to a peripheral node in all four scenarios, while f1 is only next to a peripheral node in grids (a) and (b). The location f3 is an example of a terminal fault. It is applied at node 10 on the feeder to node 1. All faults are considered to be positive pole-to-ground faults with a purely resistive constant fault impedance of 7 Ω. This value leans on findings in [27], in which a dynamic, current-dependent fault impedance model is presented.

IV. RESULTS AND DISCUSSION

A. Fault 1

The upper part of Fig. 5 shows the global maximum current through all DC CBs current in each of the four grids as a function of time after the occurrence of f1. As the fault currents approach steady-state (after approximately 300 ms), the maximum CB current in scenarios (c) and (d) is notably lower compared to those in topologies (a) and (b). The primary reason for this is that in topologies (c) and (d), the active short circuit current contributions feed the fault from two sides, reducing the maximum burden placed on individual feeders (and DC CBs).

The lower part of Fig. 5 is a magnified view of the first 6 ms of the same quantities as those shown in the upper part. In contrast to the steady-state case, in this initial transient period the maximum short circuit current is highest in topologies (c)

and (d). This is because of discharge currents from cables that connect node 1 to nodes 9 and 12, which only exist in scenarios (c) and (d). Since the fault is closest to node 1, the maximum fault DC CB current inititially occurs in the feeder from node 1 to f1 in all four topologies. In topologies (a) and (b), the CB current from node 10 to f1, i.e. $i_{10\text{-f1}}$, starts exceeding $i_{1\text{-f1}}$ shortly after the fault surge reaches node 10 (c.f. arrow on lower part of Fig. 5). The location of the maximum CB current then briefly alternates between $i_{1\text{-f1}}$ and $i_{10\text{-f1}}$, before remaining at $i_{10\text{-f1}}$ until steady-state. In topology (c), $i_{1\text{-f1}}$ remains the maximum system current until approximately 20 ms after the fault, after which $i_{10\text{-f1}}$ slightly exceeds it. Finally, in grid (d), $i_{1\text{-f1}}$ remains the maximum CB current during the entire simulation.

A snapshot of the system fault currents and DC node voltages after 5 ms (equivalent to the break time of current hybrid DC CBs [28]), is shown in Fig. 6. It further illustrates how at that particular point in time, the fault currents $i_{1\text{-f1}}$ and $i_{10\text{-f1}}$ in (a) and (b) are nearly identical, whereas in (c) and (d) $i_{1\text{-f1}}$ is clearly highest. Additionally, Fig. 6 gives the corresponding node voltages, showing that after 5 ms, in grids (a) and (c) the voltage at the remote node 6 is not yet affected by the fault, whereas in (b) and (d) it is. This difference can be attributed to the absence of the link between nodes 10 and 11 in grids (a) and (c).

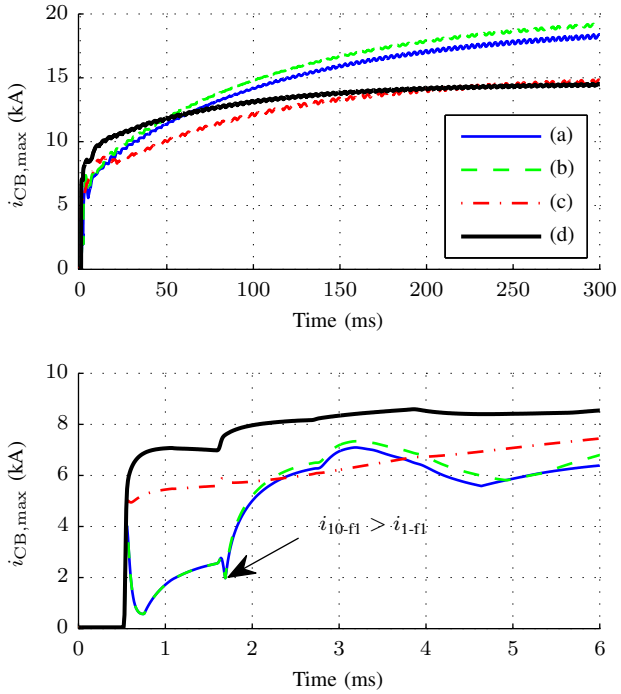

Fig. 5. Global maximum DC CB current after a fault at location f1.

B. Fault 2

In Fig. 7, the global maximum DC CB current is shown for the four different topologies. In all four scenarios, the entire grid's short circuit current is fed to f2 through the connection

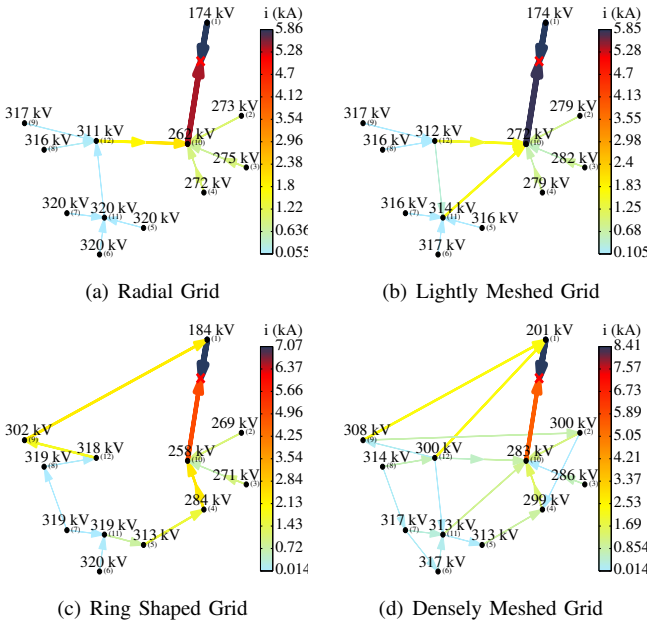

Fig. 6. System snapshot comparison of the four different grid topologies 5 ms after the occurrence of fault 1.

from node 10 (with the exception of the contribution from the peripheral node 3). Current $i_{10\text{-f2}}$ is thus clearly the maximum global DC CB current in all four scenarios (c.f. Fig. 8). Its magnitude can therefore be fully attributed to the effect of the different DC grid topologies.

As the system approaches a steady-state, the fault current contribution from the four topologies in the order of weakest to strongest is: (c) ring, (a) radial, (b) lightly meshed, (d) densely meshed. This reflects differences in the average impedance between f2 and the active fault current sources, i.e. the AC coupling points.

Another feature that stands out in Fig. 7 is the fact that the maximum CB current in grid (d) is somewhat higher than in the other three grid scenarios during the first 10 ms (c.f. lower part of Fig. 7). This is because the initial response is dominated by the discharge of cable capacitances, of which there are more in grid (d) than in the other scenarios.

Fig. 8 shows that the maximum CB current after 5 ms ranges between 9.92 kA in topology (c) and 12.7 kA in topology (d). It can also be seen that the dense mesh of topology (d) leads to voltages in Area 1 that are around 10% higher than those in the other three topologies (after 5 ms).

C. Fault 3

Fault 3 constitutes one of the worst case scenarios: a fault directly at the terminal at one of the central nodes of the network. The fault is on the same cable as f1, but directly at the bus bar of node 10.

Fig. 9 shows the global maximum CB current for the four different scenarios. It can clearly be seen that the initial rates of rise and steady-state values of the fault current are more severe compared to those in the other two fault scenarios (c.f. Fig. 5 and Fig. 7). For example, the worst case CB current

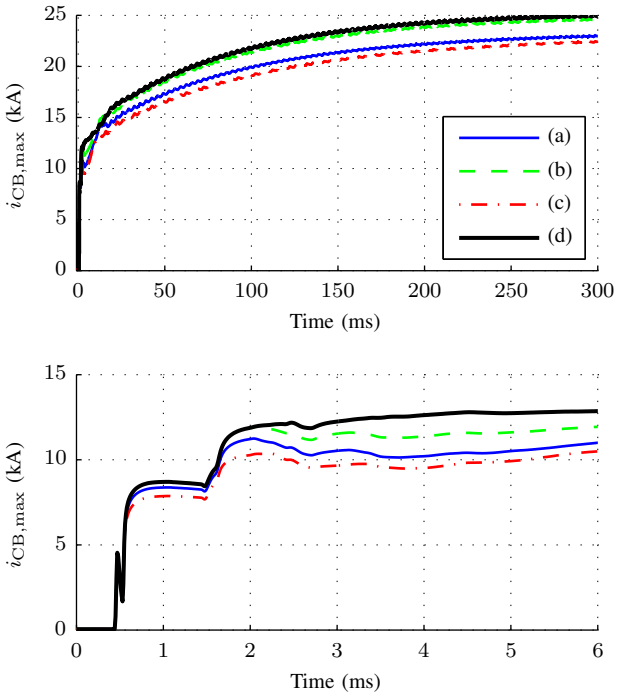

Fig. 7. Global maximum DC CB current after a fault at location f2.

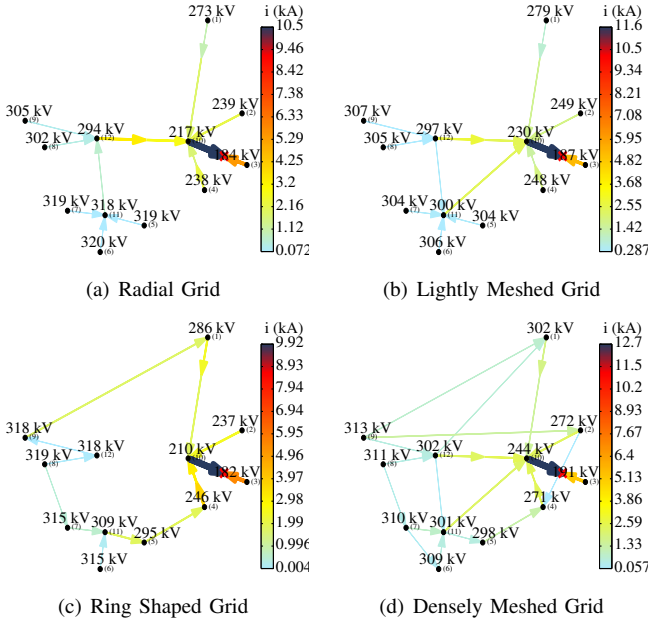

Fig. 8. System snapshot comparison of the four different grid topologies 5 ms after the occurrence of fault 2.

after 300 ms is more than 50% higher than that for f1 and more than 17% higher than for f2.

The fast rate of rise is primarily due to the near instantaneous start of discharge currents from non-faulty feeder cables connected to node 10. The higher steady-state currents are primarily due to higher AC contributions caused by the proximity to node 10 as well as to several onshore nodes.

The lower part of Fig. 9 shows that the fault current during approximately the first 1.5 ms is solely determined by the number of feeder cables connected to node 10, with the lowest fault currents for grid (c) (4 feeder cables at node 10) and the highest for grids (b) and (d) (6 feeder cables at node 10).

The differences between the four grid scenarios with regard to the steady-state fault current can be explained by the differences in the fault current distribution in the grid and differences in the impedance between other coupling points and the fault. The discontinuity in the maximum CB current after 1.5 ms (a slight increase for topology (d) and a decrease for the other three topologies) corresponds to the time when the reflection of the negative voltage wave from node 4 arrives at node 10 with a positive polarity. This leads to a sudden reduction of the contribution from this particular cable. Subsequent ripples between 1.5 ms and around 2.2 ms can similarly be attributed to the arrival of the reflected fault waves from nodes (2) and (3) (particularly notable for topology (a)). The shape of the CB current in topology (d) looks different during this phase due to different reflection coefficients at nodes 2 and 4 (due to a different number of feeders attached at these bus bars). The CB currents start to increase again at around 2.5 ms due to fault current contributions from AC nodes.

Fig. 10 shows a snapshot of the system's fault currents and DC voltages after 5 ms. It is important to note that in this figure, the global maximum system current (i.e. $i_{10\text{-}f3}$) is not represented. It illustrates the location and magnitude of the second highest line currents and gives an impression of the fault current distribution in each topology.

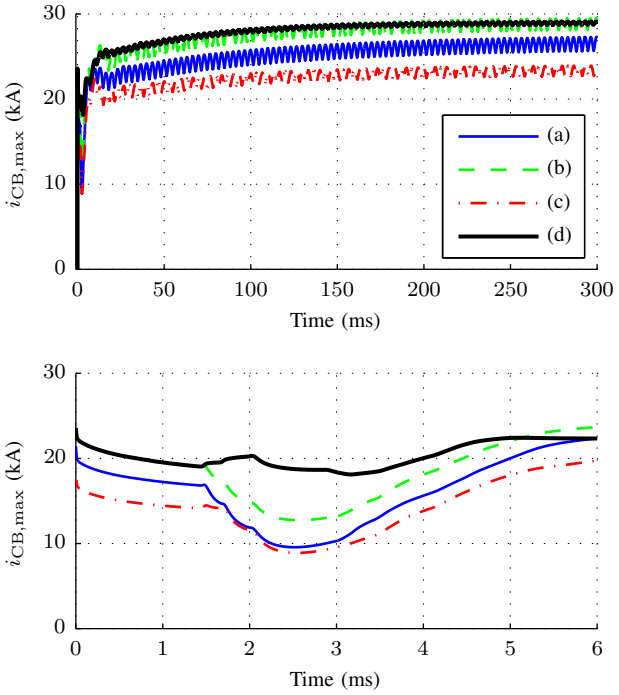

Fig. 9. Global maximum DC CB current after a fault at location f3.

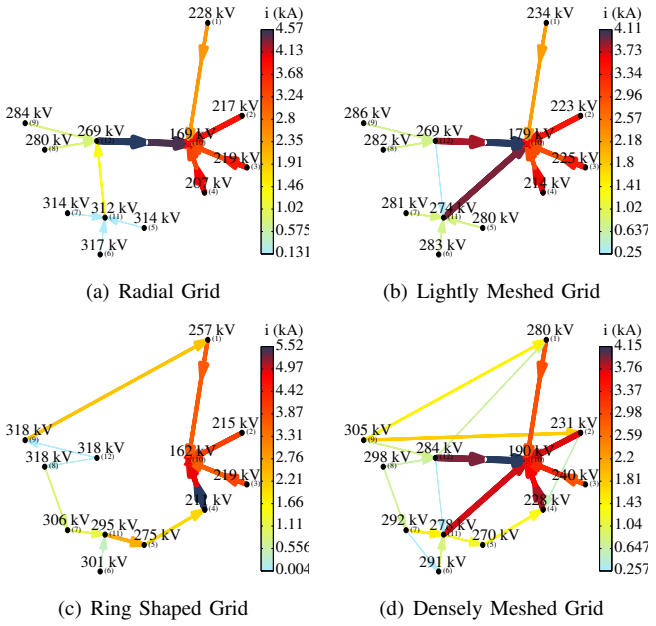

(a) Radial Grid (b) Lightly Meshed Grid

(c) Ring Shaped Grid (d) Densely Meshed Grid

Fig. 10. System snapshot comparison of the four different grid topologies 5 ms after the occurrence of fault 3.

D. Direct Comparison

Table V provides a direct comparison of the total fault current (i.e. fault-to-ground current) and the maximum CB current in the grid for the three fault locations and four grid topologies. Values are given at a time of 5 ms (equivalent to typical hybrid DC CB break time) and 50 ms (equivalent to typical mechanical resonance breaker break time).

Considering all grid topologies and fault locations, the maximum prospective CB current after 50 ms is on average 40% higher compared to that after 5 ms. Furthermore, on average, there is a 21% difference in the maximum CB current between the grid with the lowest average CB current (grid (c)) and that with the highest average CB current (grid (d)).

Another general observation that can be made is that the closer a fault is to a terminal, the higher is the ratio of the maximum CB current to the total fault current.

TABLE V
TOTAL FAULT CURRENT AND MAXIMUM DC CB CURRENT AFTER 5 AND 50 MS FOR DIFFERENT TOPOLOGIES AND FAULT LOCATIONS

	5 ms	(a)	(b)	(c)	(d)
f1	total fault current (kA)	12.38	12.65	13.07	14.87
f1	**max CB current (kA)**	**5.86**	**5.85**	**7.07**	**8.41**
f2	total fault current (kA)	15.65	16.73	15.15	17.93
f2	**max CB current (kA)**	**10.51**	**11.61**	**9.92**	**12.74**
f3	total fault current (kA)	21.11	23.08	20.30	24.76
f3	**max CB current (kA)**	**19.97**	**22.00**	**17.99**	**22.40**
	50 ms	(a)	(b)	(c)	(d)
f1	total fault current (kA)	17.53	17.97	19.55	21.51
f1	**max CB current (kA)**	**11.33**	**11.77**	**10.01**	**11.87**
f2	total fault current (kA)	22.98	23.97	22.33	24.15
f2	**max CB current (kA)**	**17.29**	**18.46**	**16.54**	**18.73**
f3	total fault current (kA)	27.61	29.62	26.42	30.02
f3	**max CB current (kA)**	**24.49**	**26.78**	**22.07**	**27.00**

V. CONCLUSION

While the choice of network topologies for future DC offshore grids will be strongly influenced by their economic merits under normal operation, the impact of the topology on the performance requirements of DC CBs cannot be neglected since the availability of technically and economically viable DC CBs is crucial for the feasibility of DC grids. Different grid topologies do not only lead to different fault current levels but, depending on the resulting distribution of fault currents in the network, also impact the maximum burden placed on individual CBs. Generally, it can be concluded that topologies that are advantageous for system redundancy and flexible trading, i.e. meshed networks, tend to be disadvantageous from a maximum fault current point of view.

For the three considered fault locations, the average maximum CB current is highest in the densely meshed grid (d), followed by the lightly meshed grid (b), the radial grid (a) and the ring shaped grid (c).

The ring shaped grid shows a favorable performance in terms of maximum CB currents because its structure leads to a favorable distribution of the fault currents for the majority of possible fault locations. Furthermore, the high impedance between different areas leads to lower average steady-state fault current levels. For the particular topologies that have been considered, the ring shaped grid offers the same level of redundancy as the lightly meshed grid (b) with respect to power transfer between areas 1, 2, and 3. A disadvantage of this topology is that, depending on the exact trading patterns, it is likely to lead to higher power losses for inter-area trading.

In general, the maximum breaking current ability of a DC CB needs to be designed primarily with regard to its own interruption time and its location in the grid. A fast interruption time is generally favorable. Shortly after the fault, fault currents are more predictable because they primarily depend on passive elements such as cable capacitances, i.e. they are independent of operating conditions of AC coupling points. Furthermore, fault currents are likely to increase over time (of course, depending on the number, strength, and distribution of AC coupling points). In the case of terminal faults, DC CBs located at busbars that connect to multiple energized cables are subject to particularly high fault currents and rates of rise. Thus, the characteristics of CBs need to be chosen according to their location in the grid. Different CB technologies and specifications may co-exist in the same network. The main parameters that need to be considered for a holisitic assessment are interruption speed, maximum breaking current, investment costs, and on-state losses.

In the future, the assessment of different topologies with regard to their fault protection requirements could be improved by considering additional fault locations and incorporating a weighting method that depends on the likelihood of occurence and impact of particular faults. Also, the assumption that IGBTs of all converter stations block instantly in the case of a fault could be further investigated in the future. Converters that are sufficiently far away from the fault may continue operating normally and their control behavior may affect the network's overall fault response. The results presented in this

paper for fault currents shortly after the fault (i.e. first 5 ms) should not be influenced by this assumption. The validity of results for longer timeframes may have to be verified with more detailed converter models with clear blocking criteria and realistic control characteristics.

VI. References

[1] L. Ronström, M. Hoffstein, R. Pajo, and M. Lahtinen, "The Estlink HVDC Light Transmission System," in *Proc. of the CIGRE Regional Meeting on Security and Reliability of Power Systems*, 2007.

[2] D. Das, J. Pan, and S. Bala, "HVDC Light for large offshore wind farm integration," in *Power Electronics and Machines in Wind Applications (PEMWA)*, Jan. 2012.

[3] J. Arrillaga, Y. Liu, and N. Watson, *Flexible Power Transmission: The HVDC Options*. John Wiley & Sons, 2007.

[4] C. Franck, "HVDC Circuit Breakers: A Review Identifying Future Research Needs," *IEEE Transactions on Power Delivery*, vol. 26, 2011.

[5] D. Jovcic, D. van Hertem, K. Linden, J.-P. Taisne, and W. Grieshaber, "Feasibility of DC Transmission Networks," in *2nd IEEE PES International Conference and Exhibition on Innovative Smart Grid Technologies (ISGT Europe)*, 2011.

[6] J. Yang, J. Fletcher, J. O'Reilly, G. Adam, and S. Fan, "Protection Scheme Design for Meshed VSC-HVDC Transmission Systems of Large-Scale Wind Farms," in *9th IET International Conference on AC and DC Power Transmission*, 2010.

[7] L. Tang and B. Ooi, "Protection of VSC-Multi-Terminal HVDC against DC Faults," in *IEEE 33rd Annual Power Electronics Specialists Conference*, 2002.

[8] J. Yang, J. Fletcher, and J. O'Reilly, "Multiterminal DC Wind Farm Collection Grid Internal Fault Analysis and Protection Design," *IEEE Transactions on Power Delivery*, vol. 25, no. 4, 2010.

[9] N. E. Link. (2013, Feb.) Estlink Project Website. [Online]. Available: http://goo.gl/IEbvl

[10] T. Worzyk, *Submarine Power Cables: Design, Installation, Repair, Environmental Aspects.* Springer Publishing Company, 2009.

[11] ABB. (2013, Feb.) HVDC Light cables, ABB. [Online]. Available: http://goo.gl/kXSte

[12] F. Mura, C. Meyer, and R. De Doncker, "Stability Analysis of High-Power DC Grids," *IEEE Transactions on Industry Applications*, vol. 46, 2010.

[13] M. Pfeiffer, "Pole-to-Ground Faults in Multi-Terminal VSC-HVDC Networks," Master's thesis, ETH Zurich, High Voltage Laboratory, 2012.

[14] J. Morren and S. de Haan, "Short-Circuit Current of Wind Turbines with Doubly Fed Induction Generator," *IEEE Transactions on Energy Conversion*, vol. 22, 2007.

[15] F. Kanellos and J. Kabouris, "Wind Farms Modeling for Short-Circuit Level Calculations in Large Power Systems," *IEEE Transactions on Power Delivery*, vol. 24, 2009.

[16] V. Gevorgian and E. Muljadi, "Wind Power Plant Short-Circuit Current Contribution for Different Fault and Wind Turbine Topologies," in *9th International Workshop on Large Scale Integration of Wind Power into Power Systems*, 2010.

[17] E. Muljadi, N. Samaan, V. Gevorgian, J. Li, and S. Pasupulati, "Short Circuit Current Contribution for Dfferent Wind Turbine Generator Types," in *IEEE Power and Energy Society General Meeting*, 2010.

[18] R. Walling, E. Gursoy, and B. English, "Current Contributions from Type 3 and Type 4 Wind Turbine Generators During Faults," in *IEEE Power and Energy Society General Meeting*, 2011.

[19] R. Nelson and H. Ma, "Short-Circuit Contributions of Full-Converter Wind Turbines," in *IEEE Power and Energy Society General Meeting*, 2011.

[20] T. Boutsika and S. Papathanassiou, "Short-Circuit Calculations in Networks with Distributed Generation," *Electric Power Systems Research*, vol. 78, 2008.

[21] Greenpeace and E. consulting. (2008) A North Sea Electricity Grid Revolution. [Online]. Available: http://goo.gl/OyVWj

[22] OffshoreGrid. (2011) Offshore Electricity Grid Infrastructure in Europe - Final Report. [Online]. Available: http://www.offshoregrid.eu/

[23] ENTSO-E. (2011) ENTSO-E Grid Map. [Online]. Available: https://www.entsoe.eu/resources/grid-map/

[24] S. Massucco and F. Silvestro, "Classification of Low Voltage Grids Based on Energy Flows and Grid Structure - Appendix: Structure and Data Concerning Ectrical Grids for Italy, Germany, Spain, UK, Poland," 2003. [Online]. Available: http://goo.gl/1BcQw

[25] P. Kundur, N. Balu, and M. Lauby, *Power System Stability and Control*. McGraw-Hill New York, 1994.

[26] M. K. Bucher, R. Wiget, G. Andersson, and C. M. Franck, "Multi-Terminal HVDC Networks - What is the Preferred Topology?" *IEEE Special Issue on HVDC Systems and Technology*, 2012, submitted for review.

[27] J. Wang, A. Liew, and M. Darveniza, "Extension of Dynamic Model of Impulse Behavior of Concentrated Grounds at High Currents," *IEEE Transactions on Power Delivery*, vol. 20, 2005.

[28] M. Callavik, A. Blomberg, J. Häfner, and B. Jacobson, "The Hybrid HVDC Breaker - An innovation breakthrough enabling reliable HVDC grids," ABB Whitepaper, Nov. 2012.